Title: Tuning commensurability in twisted van der Waals bilayers

Authors: Yanxing Li[1†], Fan Zhang[1†], Viet-Anh Ha[1, 2], Yu-Chuan Lin[3, 4], Chengye Dong[3], Qiang Gao[1], Zhida Liu[1], Xiaohui Liu[1], Sae Hee Ryu[5], Hyunsue Kim[1], Chris Jozwiak[5], Aaron Bostwick[5], Kenji Watanabe[6], Takashi Taniguchi[6], Bishoy Kousa[1], Xiaoqin Li[1], Eli Rotenberg[5], Eslam Khalaf[1], Joshua A. Robinson[3], Feliciano Giustino[1, 2], Chih-Kang Shih[1*]

[1]Department of Physics, University of Texas at Austin, Austin, USA

[2]Oden Institute for Computational Engineering and Sciences, The University of Texas at Austin, Austin, USA

[3]Department of Materials Science and Engineering, Pennsylvania State University, University Park, USA

[4]Department of Materials Science and Engineering, National Yang Ming Chiao Tung University, Hsinchu, Taiwan

[5]The Molecular Foundry, Lawrence Berkeley National Laboratory, Berkeley, USA

[6]Research Center for Materials Nanoarchitectonics, National Institute for Materials Science, Tsukuba, Japan

*Corresponding author email: shih@physics.utexas.edu

Abstract: Moiré superlattices based on van der Waals materials (vdW) bilayers are created at small twist angles leading to a long wavelength pattern with approximate translational symmetry. At large twist angles, moiré patterns are, in general, incommensurate apart from a few discrete angles. Here we show that large-angle twisted bilayers offer distinctly different new platforms. More specifically by using twisted WSe_2 bilayers, we create the incommensurate dodecagon quasicrystals (QC) at $\theta = 30°$ and the commensurate moiré crystals at $\theta = 21.8°$ or $38.2°$. Valley-resolved scanning tunneling spectroscopy (STS) unveils disparate behaviors between moiré crystals (with translational symmetry) and quasicrystals (with broken translational symmetry). In particular, the K-valley exhibits rich electronic structures exemplified by the formation of mini gaps near the valence band maximum. These discoveries demonstrate that bilayers with large twist angles offer a new design platform to explore moiré physics beyond those formed with small twist angles.

Main text:

The emergence of moiré superlattice (MSL) designed in van der Waals materials (vdW) bilayers has created unprecedented opportunities to engineer 2D electronic materials with novel properties[1–22]. Thus far, most superlattices investigated are vdW bilayers with small twist angles. At small angles, the moiré wavelength is long, and the pattern is either commensurate or nearly commensurate with the atomic lattices, thus creating a periodically modulated electronic superlattice. At large twist angles, the moiré pattern is in general incommensurate with atomic lattice except for a few angles[23–26]. The incommensurability disrupts the translational symmetry and electronic superlattice is lost. Large angle moiré structures had been largely

unexplored until the discovery of dodecagonal quasicrystal in $30°$ twisted bilayer graphene (tBLG) in 2018[27,28]. Although evidence for mini gap formations deep below the Dirac point (DP) has been observed using angle-resolved photoelectron spectroscopy (ARPES), the absence of electronic coupling near the Fermi level, E_F, has limited the effect of quasiperiodicity on other physical properties that are governed primarily by states near E_F in a metallic system. For example, quantum hall effect measurements of $30°$ tBLG show that the two layers act totally independent[29].

Here, we overcome this limitation by using WSe_2 twisted bilayers whose flatter dispersion makes the effects of quasiperiodicity more pronounced at accessible doping[30,31]. We show that large angle twisted WSe_2 bilayers offer an interesting platform to explore moiré physics beyond the MSL. We use two modes of STS, constant height and constant current, which allow us to distinguish the momentum space features arising from the K and Γ points. By contrasting the behavior of a large angle commensurate moiré crystal at $\theta_t = 21.8°/38.2°$ with the 12-fold symmetric $30°$ incommensurate moiré quasicrystal, we identify several unique properties of the latter. These include the appearance of several Umklapp scattered K-valleys and the existence of a dense set of diffraction spots that preserve the rotational symmetry without the translational symmetry. Remarkably, we are able to resolve signals associated with interlayer Umklapp scatterings up to at least third order suggesting strong interlayer hybridization. For moiré crystals, the new electronic structures are well captured by the first-principle supercell calculations. For moiré quasicrystals, we show that the dense diffraction spots facilitate electron scattering in a manner analogous to a quasi-Bragg plane that couples the Umklapp scattered K-valleys and lead to the formation of a dense set of mini gaps near the valence band maximum. These two moiré structures exemplify the new designer platform enabled at the large twist angles.

Umklapp scatterings in moiré crystal and moiré quasicrystal

Fig. 1a is the experimental schematics with two models shown below, one representing the dodecagonal quasicrystal formed with $\theta_t = 30°$, and the other one the $\sqrt{7} \times \sqrt{7}$ commensurate moiré crystal with $\theta_t = 21.8°$ (See angle determination in SI Fig. S1). STM images (Fig. 1b and c) indeed reveal the anticipated moiré quasicrystal and the moiré crystal. The corresponding Fast Fourier Transform (FFT) patterns are shown in Fig. 1d and e respectively. Fig. 1d exhibits a dense set of diffraction spots that are rotationally symmetric but without translational symmetry, which is a characteristic of the quasicrystal. By contrast, the diffraction spots of the moiré crystal, are commensurate with the atomic diffraction spots with a scaling ratio of $1/\sqrt{7}$. The dense diffraction spots in Fig. 1d can be analyzed by considering "mutual Umklapp scattering" between the upper and bottom layers, a method previously used for $30°$ tBLG[27,28] (discussed in SI, Fig. S2&3, Note 1). In our case, up to third-order Umklapp scattering can be identified. As a result, the

original K-valleys for individual layers are Umklapp scattered, creating a dense distribution of K-valleys shown in Fig. 2a. As discussed below, the electronic coupling of these K-valleys endows the rich electronic structures associated with the moiré quasicrystals. The distribution of K-valleys in the first quadrant is shown in Fig. 2b where we also label three sets of K-valley pairs (in dashed rectangles). For each pair of K-valleys, an electronic coupling will open a gap which is at the energy degenerate point (anti-crossing), and is schematically shown in Fig. 2c. Fig. 2d is the simulated density of states (DOS) near the gap using the two-band coupling model (See SI Note 2). Below the gap is a paraboloid local maximum while above the gap is a saddle point which leads to a Van Hove singularity (VHS) with logarithmic divergence in DOS. As a consequence of a dense set of diffraction spots in moiré quasicrystals, there are many K-valley pairs whose couplings can lead to anti-crossings and gap openings. One thus expects the formation of many mini gaps in moiré quasicrystals, which correspond to many VHS in DOS.

Observation of VHS from mini gaps in moiré quasicrystal

The electronic structures are investigated using valley-resolved scanning tunneling spectroscopy. Two different modes of STS are simultaneously employed: (a) the conventional constant height STS (CHSTS) and (b) the constant current STS (CCSTS). As discussed previously, K-valley states rapidly decay into the vacuum (due to a large $k_{\parallel}$) and are thus difficult to be detected using CHSTS. This difficulty in detecting the K-valley states can be overcome using the CCSTS.[32] More detailed descriptions of this method can be found in SI Note 3.

We first discuss the electronic structures for the moiré quasicrystal in Fig. 3. The STM image for the moiré quasicrystal is shown in Fig. 3a with a few spatial locations marked where tunneling spectra are acquired. The experimental condition to observe quasicrystal structure is discussed in SI Fig. S8. Shown in Fig. 3b are spectra acquired using conventional STS. The two prominent peaks correspond to the two split Γ-valleys resulting from the interlayer coupling. Here we find $\Delta_{\Gamma-\Gamma}= 0.61\ eV$, smaller than the value of $0.75\ eV$ observed in the regular R- or H-stacked bilayers (SI Fig. S9, 10). The smaller $\Delta_{\Gamma-\Gamma}$ is due to the reduction of Γ-Γ repulsion at a large twist angle. Due to the rapid decay rate of K-valley states into vacuum, they are very difficult to be detected in the CHSTS mode. In the CCSTS mode, as the sample bias is raised above the highest Γ-state, the tip-to-sample-distance (Z) is automatically adjusted to a smaller value by the feedback to detect the K-valley states (Fig. 3c). As the bias is raised above the VBM, the Z-value is reduced further and the tunneling occurs between the tip and the BLG substrate. Such Z-V plots in the constant current mode delineate different tunneling regimes (Γ-valley, K-valley, and BLG) from which the VBM can also be determined precisely. The fine spectral features in the K-valley are revealed in the differential conductivity $(\partial \mathrm{I}/\partial \mathrm{V})_{\mathrm{I}}$ (Fig. 3d-g). One can identify four sharp spectral features (peak 1-4) located at 26,

48, 93, and 154 meV below the VBM respectively (Fig. 3d). Among them, peaks 1 and 3 have a clear signature of VHS associated with saddle points above the gap while peaks 2 and 4 are interpreted as the VHS of the paraboloid below the gap (see more evidence in SI Fig. S11). At other spatial locations (Fig. 3e-g), spectra show similar structures with some sharp peaks that can be identified as saddle points. As another example in Fig. 3f, the two sharp VHS (saddle points) features occur at 36 meV and 100 meV below the VBM, coincide closely with peaks 1 and 3 in Fig. 3d. The observations of these VHS in tunneling spectra provide unambiguous signatures for the existence of mini gaps due to coupled K-valleys that are Umklapp scattered. If we further interpret peaks 2 and 4 in Fig. 3d as the energy locations below the gap, we can estimate the energy locations (and sizes) of mini gaps at 37 meV (Δ = 21 meV) and 124 meV (Δ = 60 meV) below the VBM respectively.

We have also carried out nano-ARPES (angle-resolved photoelectron spectroscopy) on exfoliated and stacked WSe_2 bilayers from which we confirm our valley assignments (Extended Data Fig. 1) and observe the band crossing of K_t and K_b occurring at 0.53 eV below the VBM (Extended Data Fig. 2). Given the fact that the energy crossing location is directly proportional to Δk^2 where Δk is the separation of two K-valleys in k-space, we can then estimate the energy locations of mini gaps due to coupling of $K_t^{1m'} - K_b^{1m'}$, $K_t - K_t^{1'}$ to be at 36$\pm$5 meV and 134$\pm$20 meV below the VBM (SI Note 4), matching quite well with the experimental observation using STS. The crossing of $K_t^{1'} - K_b^{1'}$ (at 270$\pm$41 meV below VBM) might be too close to the Γ_1 to be visible by STS. More technical details of nano-ARPES investigations are discussed in in SI Note 5.

Interlayer coherent couplings in moiré crystal

We next discuss the electronic structure for moiré crystal. The commensurate moiré structures at $\theta_t = 21.8^\circ$ and 38.2° have attracted significant interest in recent years, exemplified by the observation of coherent interlayer transport in BLG[33–35] and coherent interlayer excitons in BL-TMDs[36]. Thus far, however, STM/STS investigations had been lacking. It needs to be noted that for BLG there is no distinction between $\theta_t = 21.8^\circ$ and 38.2° because K and K' are degenerate. For BL-TMD, the situation is different because the K/K' degeneracy is lifted.

Shown in Fig. 4a is the STM image for a moiré crystal at $\theta_t = 38.2^\circ$. In our investigations, the majority (70%) of commensurate moiré structures are with $\theta_t = 38.2^\circ$ and the minority (30%) with $\theta_t = 21.8^\circ$. In addition, detailed atomic image analysis reveals isotropic strain ranging from +2% to -3% for different moiré crystals (SI Note 6). Conventional STS show similar structures as those observed in moiré quasicrystals where two Γ valleys are observable but not the K-valleys (SI Fig. S22). CCSTS (Fig. 4b), on the other hand, reveals additional structures above the upper Γ-valley. Two clear peaks (peak 1 and 2), with

60 meV separation are observed near the VBM. In addition, a weak shoulder (peak 3) is located at ~ 60 meV below peak 2. All moiré crystals show very similar spectral features regardless of $\theta_t = 21.8^\circ$ (Fig. 4c) or 38.2°. Moreover, we do not observe sharp VHS associated with saddle points.

To aid interpretation of spectral features, we carried out first-principle density functional theory (DFT) calculations. Shown in Fig. 4d are the BZs for the top layer (red), the bottom layer (blue), and the commensurate moiré structure (purple) for a $\theta_t = 21.8^\circ$ (38.2°) bilayer. A few critical points (μ, κ and κ') in the moiré BZ (MBZ) are of interest. The two K-valleys, K_t and K_b intersect at the μ point where the anti-crossing is expected. Indeed, the DFT calculation shows a gap of ~ 40 meV opening up at this point, albeit it occurs at an energy level near the Γ_1 state (Fig. 4e). At 21.8°, all K_t (K_b) valleys are Umklapp scattered to κ (κ') and thus crossing occurs only at the μ point. On the other hand, K_b' and K_t are scattered to the same κ point. At 38.2°, however, the converse is true. K_t and K_b' will intersect at μ whereas K_t and K_b would be scattered into the same κ point. If spin is conserved after Umklapp scattering, then for $\theta_t = 38.2^\circ$ bilayer, one does not expect anti-crossing occurring at μ, but a K-K splitting at κ. DFT calculations for $\theta_t = 38.2^\circ$ bilayer indeed confirm the diminishing gap at μ, but only a small K-K splitting (2 meV) at κ (SI Fig. S25). Experimental investigations in regular bilayers, nevertheless, show significant interlayer K-K coupling[37–40]. Moreover, in $MoSe_2/WS_2$ heterobilayers, splitting of moiré exciton states are found near both commensurate angles, indicating that coherent coupling exists for both $K_t - K_b$ and $K_t - K_b'$[10,41]. Another evidence for $K - K'$ coupling is also found in the quasi-particle interference (QPI) analysis (SI note 7). This mechanism provides an explanation of the observation of double peak structure near the VBM for both twisting angles. In addition, it points to a possibility that anti-crossing can also exist for both angles, albeit the energy location is too close to the Γ point to be observed by STS. Then the weak shoulder (peak 3) could be interpreted as the remanent of the VHS (saddle point) above the Γ.

In summary, we have studied twisted WSe_2 bilayers at large twist angles and discovered distinct behavior of incommensurate 12-fold rotationally symmetric 30° moiré quasicrystals and commensurate moiré crystals at 21.8°/38.2° . The former features an aperiodic long-range order which yields a dense set of diffraction spots in k-space. By combining constant height and constant current STM signals, we can resolve the spectral features arising from the K and Γ points. We observe the VHS signatures originating from several mini gaps in the quasi-periodic structure which can be explained using a coupled K-valley model with up to third Umklapp scattering suggesting strong interlayer coupling. For the commensurate 21.8°/38.2° structure, two points in the MBZ are of interest: Anti-crossing at the μ point and the coherent coupling at κ-point. The absence of VHS and the double peak structure near the VBM can be interpreted as manifestation of band structures in commensurate moiré crystals. In contrast to previously-studied 30°-

twisted bilayer graphene, the flatter dispersion of our system leads to stronger interlayer coupling at smaller bias voltage making it a very promising platform to study the physics of moiré quasicrystals at finite doping. In addition, the crystallographically-forbidden 12-fold rotation symmetry makes our system distinct from quasi-periodic multilayer moiré systems with multiple unrelated twist angle[42]. Moreover, TMD based moiré quasicrystals is a semiconductor system with strong spin-orbit coupling which endows a rich interplay of valley and spin degrees of freedom that impact both optical and transport properties. The theoretical analysis further shows that such moiré quasicrystals can be generalized to multilayer structures with higher rotation symmetry where the quasiperiodic interlayer coupling can be brought down in energy even further. For example, using tri-layers with two consecutive $20°$ twists, a new type of quasicrystal with 18-fold rotational symmetry and with an even denser set of diffraction patterns where the mini gaps are expected to occur at smaller doping (SI Fig. S29). This work provides a proof of concept for using large twist angle vdW structures as a new design platform to explore moiré physics beyond those formed at small twist angles.

References:

1. Bistritzer, R. & MacDonald, A. H. Moiré bands in twisted double-layer graphene. *Proc. Natl. Acad. Sci.* **108**, 12233–12237 (2011).
2. Zhang, C. *et al.* Interlayer couplings, Moiré patterns, and 2D electronic superlattices in MoS_2/WSe_2 hetero-bilayers. *Sci. Adv.* **3**, e1601459 (2017).
3. Cao, Y. *et al.* Correlated insulator behaviour at half-filling in magic-angle graphene superlattices. *Nature* **556**, 80–84 (2018).
4. Cao, Y. *et al.* Unconventional superconductivity in magic-angle graphene superlattices. *Nature* **556**, 43–50 (2018).
5. Jin, C. *et al.* Observation of moiré excitons in WSe2/WS2 heterostructure superlattices. *Nature* **567**, 76–80 (2019).
6. Tran, K. *et al.* Evidence for moiré excitons in van der Waals heterostructures. *Nature* **567**, 71–75 (2019).
7. Seyler, K. L. *et al.* Signatures of moiré-trapped valley excitons in MoSe2/WSe2 heterobilayers. *Nature* **567**, 66–70 (2019).
8. Lu, X. *et al.* Superconductors, orbital magnets and correlated states in magic-angle bilayer graphene. *Nature* **574**, 653–657 (2019).
9. Zhang, Z. *et al.* Flat bands in twisted bilayer transition metal dichalcogenides. *Nat. Phys.* **16**, 1093–1096 (2020).

10. Zhang, L. *et al.* Twist-angle dependence of moiré excitons in WS2/MoSe2 heterobilayers. *Nat. Commun.* **11**, 5888 (2020).
11. Wang, L. *et al.* Correlated electronic phases in twisted bilayer transition metal dichalcogenides. *Nat. Mater.* **19**, 861–866 (2020).
12. Xie, Y. *et al.* Fractional Chern insulators in magic-angle twisted bilayer graphene. *Nature* **600**, 439–443 (2021).
13. Li, H. *et al.* Imaging moiré flat bands in three-dimensional reconstructed WSe2/WS2 superlattices. *Nat. Mater.* **20**, 945–950 (2021).
14. Bai, Y. *et al.* Excitons in strain-induced one-dimensional moiré potentials at transition metal dichalcogenide heterojunctions. *Nat. Mater.* **19**, 1068–1073 (2020).
15. Sharpe, A. L. *et al.* Emergent ferromagnetism near three-quarters filling in twisted bilayer graphene. *Science* **365**, 605–608 (2019).
16. Oh, M. *et al.* Evidence for unconventional superconductivity in twisted bilayer graphene. *Nature* **600**, 240–245 (2021).
17. Li, T. *et al.* Quantum anomalous Hall effect from intertwined moiré bands. *Nature* **600**, 641–646 (2021).
18. Choi, Y. *et al.* Correlation-driven topological phases in magic-angle twisted bilayer graphene. *Nature* **589**, 536–541 (2021).
19. Wang, X. *et al.* Interfacial ferroelectricity in rhombohedral-stacked bilayer transition metal dichalcogenides. *Nat. Nanotechnol.* **17**, 367–371 (2022).
20. Törmä, P., Peotta, S. & Bernevig, B. A. Superconductivity, superfluidity and quantum geometry in twisted multilayer systems. *Nat. Rev. Phys.* **4**, 528–542 (2022).
21. Weston, A. *et al.* Interfacial ferroelectricity in marginally twisted 2D semiconductors. *Nat. Nanotechnol.* **17**, 390–395 (2022).
22. Rozhkov, A. V., Sboychakov, A. O., Rakhmanov, A. L. & Nori, F. Electronic properties of graphene-based bilayer systems. *Phys. Rep.* **648**, 1–104 (2016).
23. Lopes dos Santos, J. M. B., Peres, N. M. R. & Castro Neto, A. H. Continuum model of the twisted graphene bilayer. *Phys. Rev. B* **86**, 155449 (2012).
24. Mele, E. J. Commensuration and interlayer coherence in twisted bilayer graphene. *Phys. Rev. B* **81**, 161405 (2010).
25. Sboychakov, A. O., Rakhmanov, A. L., Rozhkov, A. V. & Nori, F. Electronic spectrum of twisted bilayer graphene. *Phys. Rev. B* **92**, 075402 (2015).

26. Rozhkov, A. V., Sboychakov, A. O., Rakhmanov, A. L. & Nori, F. Single-electron gap in the spectrum of twisted bilayer graphene. *Phys. Rev. B* **95**, 045119 (2017).
27. Ahn, S. J. *et al.* Dirac electrons in a dodecagonal graphene quasicrystal. *Science* **361**, 782–786 (2018).
28. Yao, W. *et al.* Quasicrystalline 30° twisted bilayer graphene as an incommensurate superlattice with strong interlayer coupling. *Proc. Natl. Acad. Sci.* **115**, 6928–6933 (2018).
29. Pezzini, S. *et al.* 30°-Twisted Bilayer Graphene Quasicrystals from Chemical Vapor Deposition. *Nano Lett.* **20**, 3313–3319 (2020).
30. Nguyen, P. V. *et al.* Visualizing electrostatic gating effects in two-dimensional heterostructures. *Nature* **572**, 220–223 (2019).
31. Bisri, S. Z., Shimizu, S., Nakano, M. & Iwasa, Y. Endeavor of Iontronics: From Fundamentals to Applications of Ion-Controlled Electronics. *Adv. Mater.* **29**, 1607054 (2017).
32. Zhang, C. *et al.* Probing Critical Point Energies of Transition Metal Dichalcogenides: Surprising Indirect Gap of Single Layer WSe_2. *Nano Lett.* **15**, 6494–6500 (2015).
33. Koren, E. *et al.* Coherent commensurate electronic states at the interface between misoriented graphene layers. *Nat. Nanotechnol.* **11**, 752–757 (2016).
34. Inbar, A. *et al.* The quantum twisting microscope. *Nature* **614**, 682–687 (2023).
35. Chari, T., Ribeiro-Palau, R., Dean, C. R. & Shepard, K. Resistivity of Rotated Graphite–Graphene Contacts. *Nano Lett.* **16**, 4477–4482 (2016).
36. Zhao, X. *et al.* Strong Moiré Excitons in High-Angle Twisted Transition Metal Dichalcogenide Homobilayers with Robust Commensuration. *Nano Lett.* **22**, 203–210 (2022).
37. Weston, A. *et al.* Atomic reconstruction in twisted bilayers of transition metal dichalcogenides. *Nat. Nanotechnol.* **15**, 592–597 (2020).
38. McCreary, K. M. *et al.* Stacking-dependent optical properties in bilayer WSe_2. *Nanoscale* **14**, 147–156 (2022).
39. Hsu, W.-T. *et al.* Quantitative determination of interlayer electronic coupling at various critical points in bilayer Mo S 2. *Phys. Rev. B* **106**, 125302 (2022).
40. Hsu, W.-T. *et al.* Tailoring excitonic states of van der Waals bilayers through stacking configuration, band alignment, and valley spin. *Sci. Adv.* **5**, eaax7407 (2019).
41. Zhang, Y., Devakul, T. & Fu, L. Spin-textured Chern bands in AB-stacked transition metal dichalcogenide bilayers. *Proc. Natl. Acad. Sci.* **118**, e2112673118 (2021).
42. Uri, A. *et al.* Superconductivity and strong interactions in a tunable moiré quasiperiodic crystal. Preprint at http://arxiv.org/abs/2302.00686 (2023).

Figure captions:

Figure 1 | WSe_2 commensurate moiré crystal and incommensurate moiré quasicrystal. a, Top: Schematics of the experimental set-up. Bottom: the simulated patterns for 30° incommensurate quasicrystal and 21.8° commensurate moiré crystal. **b,** Typical STM topography for 30° incommensurate quasicrystal (V_{Bias} = 0.3V, I = 30pA). **c,** Typical STM topography for 21.8° commensurate moiré. (V_{Bias} = -0.6V, I = -20pA). **d,** The FFT image of the quasicrystal topography in b with a 6-fold rotational symmetrization. The red circles mark the 12-fold dodecagonal pattern. **e,** The FFT image of the 21.8° commensurate moiré topography in c with a 6-fold rotational symmetrization. The outer and inner dashed hexagons mark the frequency peaks of the WSe_2 reciprocal lattice vectors for the Bragg lattice and commensurate moiré crystal, respectively.

Figure 2 | Umklapp scatterings and mini gap formation. a, The schematic of the first 3 orders of Umklapp scatterings near the first BZ for 30° quasicrystal. The red and blue hexagons mark the top and bottom Brillouin zones respectively. The red and blue color dots and circles represent the original K(K') valleys or Umklapp scattered K(K') replicas originated from top and bottom layers respectively. **b,** The distribution of K-valleys in the first quadrant. Three sets of K-valley pair whose couplings can lead to anti-crossing and gap opening are marked in dashed rectangles. **c,** Schematic of a 3D band dispersion showing a mini gap formed by K-valleys' anti-crossing. Where the white and yellow dashed lines represent the gapped band structures in k_x and k_y direction in the momentum space respectively. **d,** Simulated density of states as a function of energy for a typical mini gap. The upper band edge (saddle point) corresponds to a sharp VHS with logarithmic divergence while the lower edge (paraboloid) corresponds to a weak VHS.

Figure 3 | Observation of VHS in 30° moiré quasicrystal. a, STM topography image for a typical 30° quasicrystal region. The black dots mark the sites of the measurement respectively (V_{Bias} = -0.75 V, I = -20 pA). **b,** Large scale and zoom-in (inset) regular constant height *dI/dV* spectroscopies taken from sites 1 to 4. The light blue arrow and blue arrow mark the Γ_2, Γ_1, respectively (V_{Bias} = -2.0 V / -1.2 V, I = -50 pA / -200 pA). **c,** Zoom-in ZV spectroscopies from sites 1 to 4 (I = -30 pA). **d-g,** Constant current $\partial I/\partial V$ spectroscopies respectively on site 1-4. All peak (shoulder) locations above Γ_1 are marked by red dashed lines. The location of K_{VBM} is indicated with a black dash line (V_{int} = -1.2 V, I = -30 pA, V_{amp} = 10 mV).

Figure 4 | Interlayer couplings in $21.8°/38.2°$ commensurate moiré crystal. a, STM topography image for a typical 38.2° commensurate moiré crystal region (V_{Bias} = -0.5 V, I = -20 pA). **b,** Gaussian peak fittings for a zoom-in constant current $\partial I/\partial V$ spectroscopies at 38.2° twisted region. The dashed curves represent the fitted peaks (V_{int} = -1.2 V, I = -20 pA, V_{amp} = 15 mV). **c,** Gaussian peak fittings for a zoom-in constant current $\partial I/\partial V$ spectroscopies at 21.8° twisted region. The dashed curves represent the fitted peaks (V_{int} = -1.2 V, I = -20 pA, V_{amp} = 15 mV). **d,**

Schematic on the left showing the first Brillouin zones (BZs) for 21.8°(38.2°) twisted WSe_2 bilayer. The purple, red and black hexagons mark the moiré BZs, top and bottom layer BZs respectively. The K_t, K_t' and K_b, K_b' points of the top (bottom) layer BZ are respectively marked with red and blue circles, $\kappa(\kappa')$ points are marked with purple circles. Schematics on the right show the anti-crossing coupling happened at μ and the coherent coupling at $\kappa(\kappa')$. **e,** DFT calculated unfolded band structure of 21.8° commensurate moiré along the *k*-space path: $\Gamma - K_t - K_b - K_t' - \kappa' - \kappa - \Gamma$. Inset: zoom-in band structure of K_t and K_b band-crossing showing the mini gap.

Methods

Sample growth

High-quality buffer on SiC was synthesized via a two-step process. First, monolayer epitaxial graphene was synthesized via silicon sublimation from Si face of semi-insulating SiC substrates (II-VI Inc.). Prior to the growth, SiC substrates were annealed in 10% hydrogen (balance argon) at 1500 ℃ for 30 min to remove subsurface damages due to the chemical and mechanical polishing. Then monolayer epitaxial graphene (MLEG) was formed at 1800 ℃ for 30 min in a pure argon atmosphere. Second, Ni stressor layer was employed to exfoliate the top graphene layer to obtain fresh and high-quality buffer on SiC. 270 nm Ni was e-beam deposited on MLEG with a rate of 5 $\text{Å}/s$ as a stressor layer. Then thermal release tape was used to peel off the top graphene layer from the substrate. The growth of WSe_2 crystals on an EG substrate was carried out at 800 °C in a custom-built vertical cold-wall chemical vapor deposition (CVD) reactor for 20 minutes[43]. The tungsten hexacarbonyl ($W(CO)_6$) (99.99%, Sigma-Aldrich) source was kept inside a stainless-steel bubbler where the temperature and pressure of the bubbler were always held at 37 °C and 730 Torr, respectively. Mass flow controllers were used to supply H_2 carrier gas to the bubbler to transport $W(CO)_6$ precursor into the CVD chamber. The flow rate of the H_2 gas through the bubbler was maintained at a constant 8 sccm (standard cubic centimeters per minute) which resulted in a $W(CO)_6$ flow rate of 9.0×10^{-4} sccm at the outlet of the bubbler. H_2Se (99.99%, Matheson) gas was supplied from a separate gas manifold and introduced at the inlet of the reactor at a constant flow rate of 30 sccm.

STM/STS measurements

Scanning Tunneling Microscopy and Spectroscopy (STM/S) measurements were conducted at 4.3 K in the STM chamber, with a base pressure$\sim 10^{-11}$ Torr. The W tip was prepared by electrochemical etching and then cleaned by in situ electron-beam heating. STM dI/dV spectra were measured using a standard lock-in technique, whose modulation frequency is 758 Hz. Two different modes of STS were simultaneously employed: (a) the conventional constant height STS (CHSTS) and (b) the constant current STS (CCSTS).

Sample fabrication for nano-ARPES measurements

WSe_2 monolayers, bilayers and hBN layers were exfoliated from high-quality bulk crystals. We use the tear-and-stack method to control the twist angle with an accuracy better than 0.1°. The thickness of bottom hBN layers in all samples is around 3 nm, according to AFM measurements. All samples are firstly annealed at 300 ℃ in an MBE chamber for 30 min with sufficient Se pressure and then annealed at 250 ℃ in an UHV ($\sim 1 \times 10^{-10}\ Torr$) chamber before the ARPES measurement.

nano-ARPES measurements

The experimental setup utilized in this study involved the implementation of nano-ARPES (nano-Angle-Resolved PhotoEmission Spectroscopy) to investigate the electronic structure of the sample. NanoARPES measurements were conducted at the MAESTRO beamline at the Advanced Light source. A capillary mirror obtained from Sigray was employed to achieve a beam size of approximately 1 μm. The measurements were performed at a temperature of approximately 20 K with the R4000 analyzer, equipped with a custom electron deflector, and photon energy of 150 eV was employed during the experiments. To identify the target region, XY scans were conducted with a step size of 0.5 μm. The thickness and the rotation angle of the sample was determined by comparing the intensity of the core level spectrum of O 2s obtained from the natively oxidized silicon substrate, and the valence band structure of the sample.

Theoretical calculation

The Density Functional Theory (DFT) calculations were implemented in the Quantum ESPRESSO suite.[44,45] We employed the PBE exchange-correlation functional[46] in all DFT calculations. The structural optimization was obtained with criteria for force < 0.025 eV/Å, pressure < 0.5 kbar, and total energy < 0.0014 eV. We utilized optimized norm-conserving pseudopotentials[47] from the PseudoDojo library[48] with planewaves kinetic energy cutoff of 98 Ry as recommended. The Van der Waals interaction was taken into account within the semiempirical approach Grimme-D3.[49] The spin-orbit coupling was also included. The unfolded band structures were performed using BandUP code.[50–52]

Method references

43. Lin, Y.-C. *et al.* Realizing Large-Scale, Electronic-Grade Two-Dimensional Semiconductors. *ACS Nano* **12**, 965–975 (2018).
44. Giannozzi, P. *et al.* QUANTUM ESPRESSO: a modular and open-source software project for quantum simulations of materials. *J. Phys. Condens. Matter* **21**, 395502 (2009).
45. Giannozzi, P. *et al.* Advanced capabilities for materials modelling with Quantum ESPRESSO. *J. Phys. Condens. Matter* **29**, 465901 (2017).
46. Perdew, J. P., Burke, K. & Ernzerhof, M. Generalized Gradient Approximation Made Simple. *Phys. Rev. Lett.* **77**, 3865–3868 (1996).

47. Hamann, D. R. Optimized norm-conserving Vanderbilt pseudopotentials. *Phys. Rev. B* **88**, 085117 (2013).
48. van Setten, M. J. *et al.* The PseudoDojo: Training and grading a 85 element optimized norm-conserving pseudopotential table. *Comput. Phys. Commun.* **226**, 39–54 (2018).
49. Grimme, S., Antony, J., Ehrlich, S. & Krieg, H. A consistent and accurate *ab initio* parametrization of density functional dispersion correction (DFT-D) for the 94 elements H-Pu. *J. Chem. Phys.* **132**, 154104 (2010).
50. Medeiros, P. V. C., Stafström, S. & Björk, J. Effects of extrinsic and intrinsic perturbations on the electronic structure of graphene: Retaining an effective primitive cell band structure by band unfolding. *Phys. Rev. B* **89**, 041407 (2014).
51. Medeiros, P. V. C., Tsirkin, S. S., Stafström, S. & Björk, J. Unfolding spinor wave functions and expectation values of general operators: Introducing the unfolding-density operator. *Phys. Rev. B* **91**, 041116 (2015).
52. Iraola, M. *et al.* IrRep: Symmetry eigenvalues and irreducible representations of ab initio band structures. *Comput. Phys. Commun.* **272**, 108226 (2022).

Acknowledgments: This work was primarily supported by the NSF through the Center for Dynamics and Control of Materials: an NSF Materials Research Science and Engineering Center under cooperative agreement nos. DMR-1720595, DMR-2308817 and the US Air Force grant no. FA2386-21-1-4061. Other supports were from NSF grant nos. DMR-1808751, DMR-2219610, and the Welch Foundation F-2164. V.-A. Ha and F. Giustino were supported by the Welch foundation Grant No. F-2139-20230405 and the National Science Foundation Grant No. 2103991. V.-A.H. and F.G. used resources of the National Energy Research Scientific Computing Center and the Argonne Leadership Computing Facility, which are DOE Office of Science User Facilities supported by the Office of Science of the U.S. Department of Energy, under Contracts No. DE-AC02-05CH11231 and DE-AC02-06CH11357, respectively. V.-A.H. and F.G. acknowledge the Texas Advanced Computing Center (TACC) at The University of Texas at Austin for providing access to Frontera, Lonestar6, and Texascale Days, that have contributed to the research results reported within this paper (http://www.tacc.utexas.edu). Work at Penn State University was supported by the Penn State Center for Nanoscale Science (NSF Grant DMR-2011839) and the Penn State 2DCC-MIP (NSF DMR-1539916). E. R. and S. H. R. acknowledge funding of the QSA, supported by the U.S. Department of Energy, Office of Science, National Quantum Information Science Research Centers. This research used resources of the Advanced Light Source, which is a DOE Office of Science User Facility under contract no. DE-AC02-05CH11231. Z. L., X. L. and X. Li gratefully acknowledge support from the National Science Foundation via grant NSF ECCS-2130552, the Department of Energy, Office of Basic Energy Sciences under grant DE-SC0019398 and the Welch Foundation grant F-1662. K.W. and T.T. acknowledge support from the JSPS KAKENHI (Grant Numbers 20H00354, 21H05233 and 23H02052) and World Premier International Research Center Initiative (WPI), NEXT, Japan.

Author contributions: C.K.S. conceived the experiment. Y.L. and F.Z. carried out STM/STS measurements. V.H. and F.G. performed DFT calculations. Y.L., C.D., and J.A.R. prepared the MOCVD sample. H.K. helped anneal the sample and perform LEED measurements. Q.G., B.K., and E.K. performed theoretical model calculations. Z. L. and X. Liu. prepared the exfoliated sample. X. Li. involved in the discussion. K.W. and T.T. synthesized the hBN bulk crystals. S. H. R. and E.R. performed the nano ARPES measurement and analyzed the ARPES data. C. J. and A. B. helped with the nano ARPES setup. Y.L., F.Z., and C.K.S. analyzed the STM data. Y.L., F.Z. and C.K.S. wrote the manuscript with substantial contributions from all the authors. [†]These authors contribute equally to this work.

Competing Interests: All the authors declare no competing interests.

Data Availability: Source data that reproduces the plots in the main text and extended data figures are provided with this paper. Source data that reproduce the plots in supplementary information are available upon request.

Code Availability: Source codes used in the manuscript are provided with the paper. The DFT calculations presented in the paper were carried out using publicly available electronic structure codes (referenced in Methods). All other codes in supplementary information are available upon reasonable request.

Extended Data Figure captions

Extended Data Figure 1 | Comparison of valley assignments between CCSTS and nano-ARPES. a, The zoom-in CCSTS taken on quasicrystal. (same as Fig. 3d) **b,** The zoom in K-valley spectrum from the nano-ARPES measurements. **c,** The zoom in Γ-valley spectrum from the nano-ARPES measurements.

Extended Data Figure 2 | nano-ARPES results for quasicrystal. a, The constant energy surface at E = -1.9 eV. The trigonal K-valleys are labeled by the blue and red solid dots. The blue and red hole circles label the expected locations of the 1st-order Umklapp scatterings. However, no clear features of Umklapp replicas are observed. **b,** Energy distribution curve (EDC) across the center of Γ. Two peaks represent Γ_1 (-1.97 eV) and Γ_2 (-2.44 eV) respectively. **c,** The measured band structure across the center of Γ (k_y=0 Å^{-1}). **d,** The measured band structure across the center of K (k_y=-0.4 Å^{-1}), the K_{VBM} is estimated to be at -1.7 eV. **e,** The measured band structure along the K_t-K_b direction (k_x=-1.4 Å^{-1}) shows the bands crossing. The energy level of the crossing point is determined by the saddle point, at E = -2.23 eV.

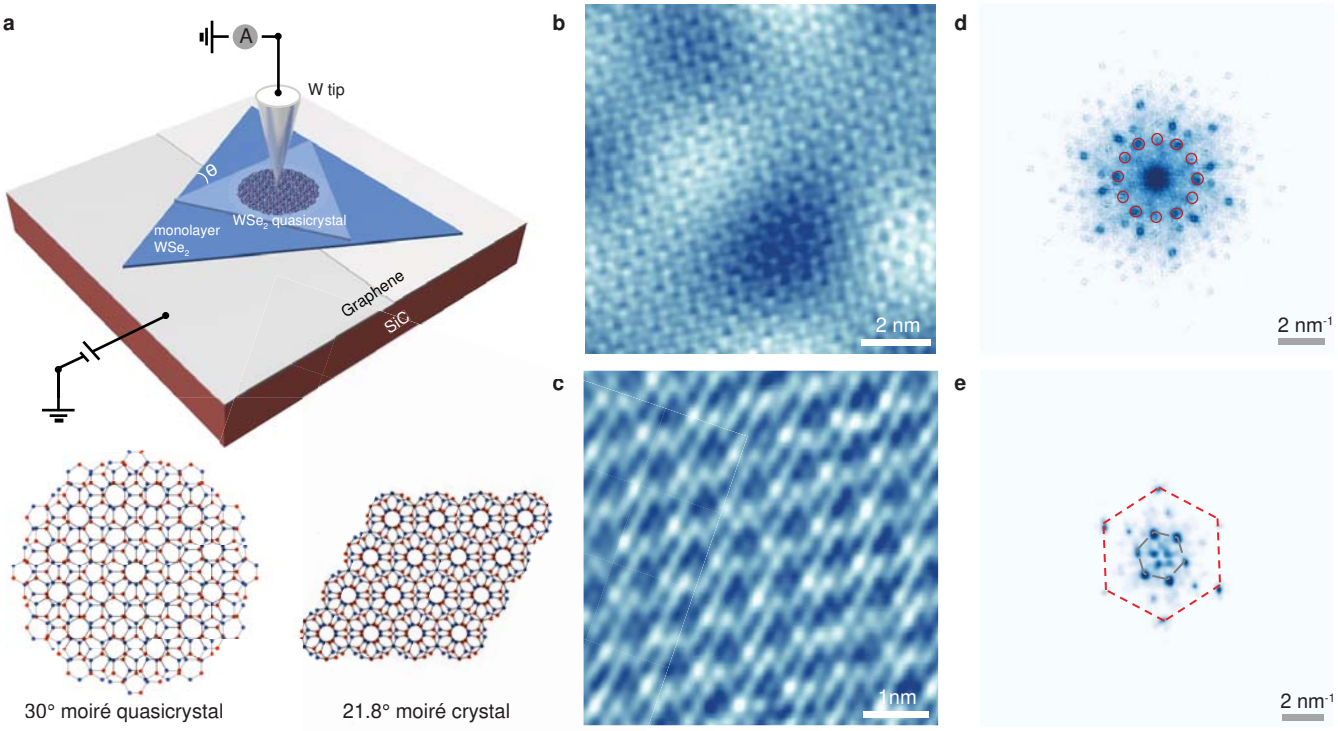
a
A
W tip
θ
monolayer
WSe2
WSe2 quasicrystal
Graphene
SiC
30° moiré quasicrystal
21.8° moiré crystal
b
2 nm
c
1nm
d
2 nm-1
e
2 nm-1

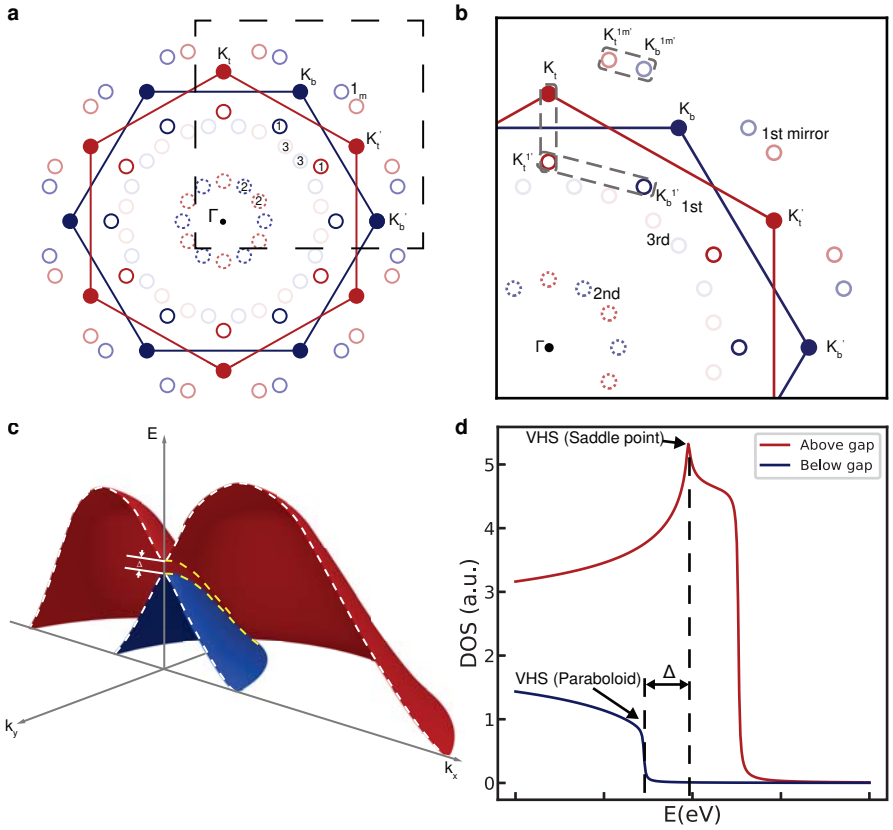
a
b
c
d
Γ
1st mirror
1st
2nd
3rd
E
VHS (Saddle point)
VHS (Paraboloid)
Above gap
Below gap
DOS (a.u.)
E(eV)

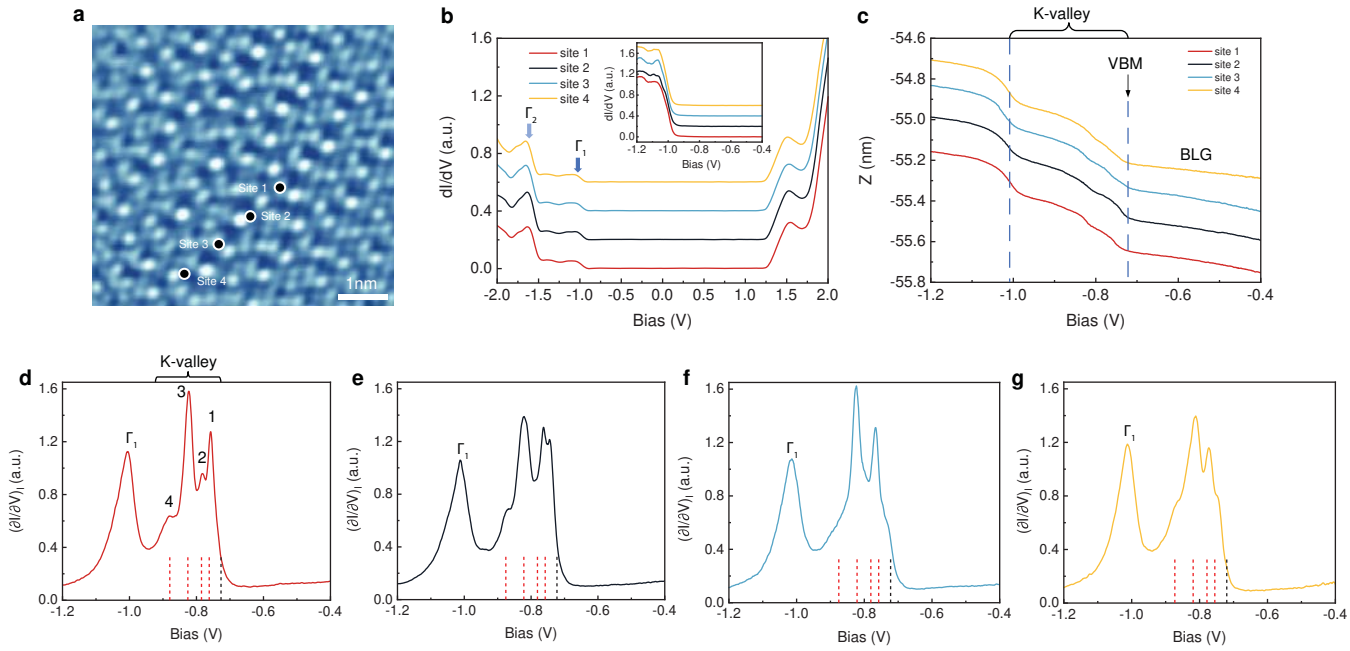
a
Site 1
Site 2
Site 3
Site 4
1nm
b
site 1
site 2
site 3
site 4
Γ2
Γ1
dI/dV (a.u.)
Bias (V)
c
K-valley
VBM
BLG
site 1
site 2
site 3
site 4
Z (nm)
Bias (V)
d
K-valley
Γ1
1
2
3
4
(dI/dV)| (a.u.)
Bias (V)
e
Γ1
(dI/dV)| (a.u.)
Bias (V)
f
Γ1
(dI/dV)| (a.u.)
Bias (V)
g
Γ1
(dI/dV)| (a.u.)
Bias (V)

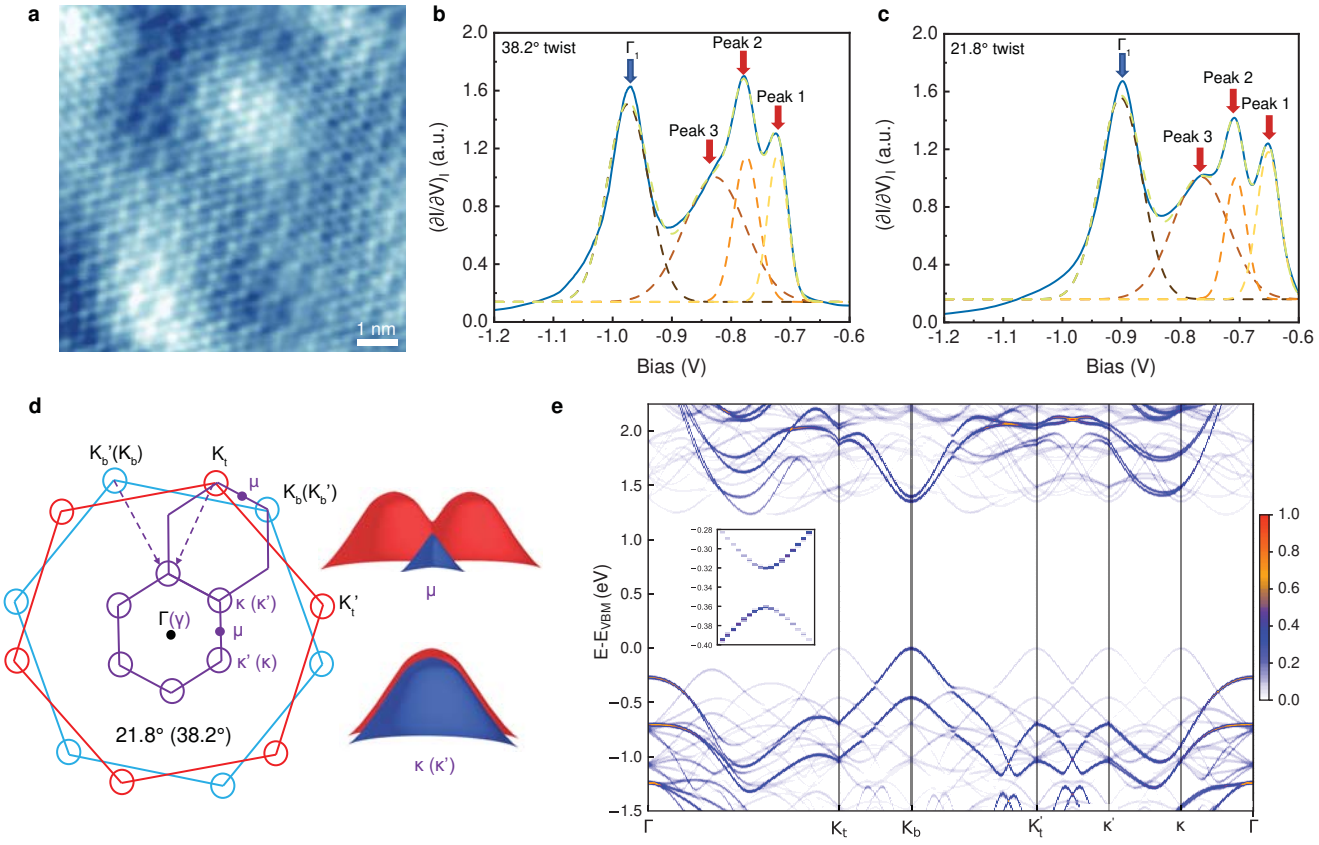
a
1 nm
b
38.2° twist
Γ1
Peak 2
Peak 1
Peak 3
(∂I/∂V)I (a.u.)
Bias (V)
c
21.8° twist
Γ1
Peak 2
Peak 1
Peak 3
(∂I/∂V)I (a.u.)
Bias (V)
d
Kb'(Kb)
Kt
μ
Kb(Kb')
Kt'
Γ(γ)
κ (κ')
μ
κ' (κ)
21.8° (38.2°)
μ
κ (κ')
e
E-EVBM (eV)
Γ
Kt
Kb
Kt'
κ'
κ
Γ